Fractal Modeling and Segmentation for the Enhancement of Microcalcifications in Digital Mammograms

Huai Li, *Member, IEEE*, K. J. Ray Liu,* *Senior Member, IEEE*, and Shih-Chung B. Lo, *Member, IEEE*

***Abstract*—The objective of this research is to model the mammographic parenchymal, ductal patterns and enhance the microcalcifications using deterministic fractal approach. According to the theory of deterministic fractal geometry, images can be modeled by deterministic fractal objects which are attractors of sets of two-dimensional (2-D) affine transformations. The iterated functions systems and the collage theorem are the mathematical foundations of fractal image modeling. In this paper, a methodology based on fractal image modeling is developed to analyze and model breast background structures. We show that general mammographic parenchymal and ductal patterns can be well modeled by a set of parameters of affine transformations. Therefore, microcalcifications can be enhanced by taking the difference between the original image and the modeled image. Our results are compared with those of the partial wavelet reconstruction and morphological operation approaches. The results demonstrate that the fractal modeling method is an effective way to enhance microcalcifications. It may also be able to improve the detection and classification of microcalcifications in a computer-aided diagnosis system.**

***Index Terms*—Enhancement, fractal modeling, mammograms, microcalcifications.**

I. Introduction

BREAST cancer is the most frequently occurring cancer and one of the leading causes of death among women [1], [2]. However, there is clear evidence that early diagnosis and subsequent treatment can significantly improve the chance of survival for patients with breast cancer [1]–[4]. Mammography is the most effective method for the detection of early breast cancer [2], [4]. But studies have shown that radiologists do not detect all breast cancers that are retrospectively detected on the mammograms [5], [6]. Because of the subtle and complex nature of the radiographic findings associated with breast cancer, errors in radiological diagnosis can be attributed to human factors such as varying decision criteria, distraction by other image features, and simple oversight. Studies suggest that these errors may occur even with experienced radiologists [5], [6]. In order to increase diagnostic efficiency, computer-assisted schemes based on advanced image processing and pattern recognition techniques can be used to locate and classify possible lesions, thereby alerting the radiologist to examine these areas with particular attention. Moreover, these computer-assisted schemes can improve the performance of the automatic computer-aided diagnosis systems, which can serve as a "prereader" to the radiologist and give the radiologist the "second opinion" in the diagnosis.

Microcalcifications are considered to be important signs of breast cancer. It has been reported that 30–50% of breast cancers detected radiographically demonstrate microcalcifications on mammograms [7], and 60–80% of breast carcinomas reveal microcalcifications upon histologic examinations [8]. The high correlation between the presence of microcalcifications and the presence of breast cancers indicates that accurate detection of microcalcifications will improve the efficacy of mammography as a diagnostic procedure. The task of detection of microcalcifications for the diagnosis of breast cancer is a difficult one. Dense breasts, improper technical factors, or simple oversight by radiologists may contribute to the failure of detecting microcalcifications.

Given a mammogram, there are three major problems in analyzing and detecting microcalcifications.

1) Microcalcifications are very small. On mammograms, they appear as tiny objects which can be described as granular, linear, or irregular. According to the literature, the sizes of microcalcifications are from 0.1–1.0 mm, and the average diameter is about 0.3 mm [7]. Small ones (ranging 0.1–0.2 mm) can hardly be seen on the mammogram due to their superimposition on the breast parenchymal textures and noise.
2) Microcalcifications often appear in an inhomogeneous background describing the structure of the breast tissue. Some parts of the background, such as dense tissue, may be brighter than the microcalcifications in the fatty part of the breast.
3) Some microcalcifications have low contrast to the background. In other words, the intensity and size of the microcalcifications can be very close to noise or the inhomogeneous background.

The above reasons make microcalcifications relatively difficult to detect. Especially, some subtle case, such as faint

Manuscript received April 15, 1996; revised March 25, 1997. This work was supported in part by the National Science Foundation under NYI Award MIP-9457397 and the U. S. Army under Grant DAMD17-93-J-3007. The Associate Editor responsible for coordinating the review of this paper and recommending its publication was L. P. Clarke. *Asterisk indicates corresponding author.*

H. Li is with the Odyssey Technologies Inc., Jessup, MD 20794 USA.

*K. J. R. Liu is with the Department of Electrical Engineering, University of Maryland at College Park, College Park, MD 20742 USA (e-mail: kjrliu@eng.umd.edu).

S.-C. B. Lo is with the Department of Radiology, Georgetown University Medical Center, Washington, DC 20007 USA.

Publisher Item Identifier S 0278-0062(97)08961-1.

microcalcifications which have small sizes and are superimposed on dense breast regions, are very difficult to detect, even for experienced radiologists. Consequently, computer-assisted detection of microcalcifications has aroused a great deal of interest. Different approaches have been proposed for enhancing and segmenting microcalcifications, including various filtering and local thresholding methods [9]–[12], mathematical morphology [13], [14], neural networks [15]–[17], the stochastic models [18], [19], the stochastic fractal model [20], pyramidal multiresolution image representation [21]–[23], and the contour-based approach [24]. We noted that most of the enhancement techniques used in the past research works not only enhanced microcalcifications, but also enhanced background structure and noise. Our basic idea is that if we can tell the different properties of disease patterns (such as microcalcifications) and background patterns in both spatial and frequency domains, then we can separate the whole image into different layers using different models according to the difference in patterns. One layer only contains disease pattern information. The other layer contains nondisease related background information. Hence, the disease pattern will be enhanced by taking the background layer from the original image. In our previous study, we employed partial wavelet reconstruction and morphological operation to remove the background information, thereby enhancing microcalcifications. The results were used to test the computer-aided diagnosis system (CADx), and improved the performance of CADx [15].

Recently, both stochastic and deterministic fractal-based techniques have been applied in many areas of digital image processing, such as image segmentation, image analysis [20], [30]–[33], image synthesis, computer graphics [34], [35], [38], and texture coding [36], [37]. Based on the deterministic fractal theory, images can be modeled by deterministic fractal objects which are attractors of sets of two-dimensional (2-D) affine transformations [38], [40], [41]. In other words, image context can be constructed by a set of model parameters which require fewer bits to describe than the original image. The mathematical theory of iterated function systems (IFS), along with the "collage theorem," constitutes the broad foundations of fractal modeling and coding. In this work, we propose the deterministic fractal model to model the mammographic background and to enhance microcalcifications. We observed that microcalcifications are visible as small objects which appear to be added to the mammographic background. Some of them are bright, some are faint. Microcalcifications can be characterized as different shapes. But compared with breast background tissue, they have less structure. On the other hand, the mammographic parenchymal and ductal patterns in mammograms possess structures with high local self-similarity which is the basic property of fractal objects. These tissue patterns can be constructed by fractal models, and be taken out from the original image, as such the microcalcification information will be enhanced. The results are very encouraging compared with those of partial wavelet reconstruction and morphological operation methods. We anticipate that the proposed fractal approach is very helpful for radiologists to detect the microcalcifications, and also facilitates the evaluation procedures in a mammographic computer-aided diagnosis system.

The remainder of this paper is organized as follows. In Section II, the general enhancement techniques and the idea behind our enhancement scheme are described. The theory and algorithm of fractal modeling are presented in Section III. Also, in this section, the enhancement of microcalcifications based on fractal modeling approach is formulated. Evaluation results are given and discussed in Section IV. Finally, this paper is summarized in Section V.

II. Enhancement Techniques

Image enhancement refers to attenuation, or sharpening, of image features such as edges, boundaries, or contrast to make the processed image more useful for analysis. Image enhancement includes gray-level and contrast manipulation, noise reduction, background removal, edge crisping and sharpening, filtering, interpolation and magnification, pseudocoloring, and so on. For a specific application, the enhancement technique used may be different. The greatest difficulty in image enhancement is quantifying the evaluation criteria for enhancement. Image enhancement techniques can be improved if the enhancement criteria can be stated precisely. Often such criteria are application dependent. In the following, we summarize general enhancement techniques used in mammographic images, and in Section III we describe our proposed fractal approach to the enhancement of microcalcifications, which are the important disease pattern on mammograms. The definitions of the criteria used in our study and more detail explanation of using these criteria are given in Section IV.

A. Conventional Enhancement Techniques

Unsharp masking [26], spatial filtering [27], region-based contrast enhancement [29], and multiscale analysis [23] are the most useful techniques to enhance mammographic features. But, most of the enhancement techniques used in past research enhanced not only microcalcifications, but also background structure and noise. Therefore, these kinds of enhancement were not microcalcification-oriented.

1) Enhancement by Contrast Stretching: The simplest method of increasing the contrast in a mammogram is to adjust the mammogram histogram so that there is a greater separation between foreground and background gray-level distributions. Denoting the input image gray level by x, and the output gray-scale values by y, the rescaling transformation is $y = f(x)$, where $f(\cdot)$ can be any designing function. Equation (1) shows a typical contrast stretching transformation of the gray-level distribution in the mammogram [42]

$$y = \begin{cases} \alpha x, & 0 \le x < a \\ \beta(x-a) + y_a, & a \le x < b \\ \gamma(x-b) + y_b, & b \le x < L \end{cases} \tag{1}$$

where the slope α, β, and γ are chosen greater than unity in the region of stretch, the parameters a and b can be obtained by examining the histogram of the original mammogram, and L is the maximum gray level of the original mammogram.

2) Enhancement by Histogram Modeling: Histogram modeling techniques modify an image so that its histogram has a desired shape. This is useful in stretching the low contrast levels of mammograms with narrow histograms. A typical technique in histogram modeling is histogram equalization. Let us consider the mammogram histogram as a probability distribution. Based on the information theory, the uniform distribution achieves the maximum entropy which contains the most information. Therefore, if we redistribute the gray levels to obtain a histogram as uniform as possible, the mammogram information should be maximized [25], [42].

3) Convolution Mask Enhancement: Convolutional masking is one of the most commonly used methods for mammogram enhancement. Unsharp masking and Sobel-gradient operations are two examples. The processed image is sharper because low-frequency information in the mammogram is reduced in intensity while high-frequency details are amplified [26], [27].

4) Fixed-Neighborhood Statistical Enhancement: The enhancement techniques we stated above are global-based approaches. For some mammograms which contain inhomogeneous background, local-based enhancement techniques can have better performance. Local enhancement techniques use statistical properties in the neighborhood of a pixel to estimate the background, suppress it, and increase local contrast [28].

5) Region-Based Enhancement: The above techniques can all be classified as either fixed-neighborhood or global techniques. They may adapt to local features within a neighborhood, but do not adapt the size of the neighborhood to local properties. Many medical images, including mammograms, possess clinically defined image features within a region of interest. These features can vary widely in size and shape, and often cannot be enhanced by fixed-neighborhood or global techniques. Thus, there is a need for adaptive-neighborhood techniques which adaptively change the size of regions in a given image and enhance the regions with respect to their local background [29].

B. Enhancement by Background Removal

In this paper, our goal is to enhance the visibility and detectability of microcalcifications. Background removal is considered a necessary procedure. Background removal is a direct method of reducing the slowly varying portions of an image, which in turn allows increased gray-level variation in image details. It is usually performed by subtracting a low-pass filtered version of the image from itself. Morphological processing [13] and partial wavelet reconstruction [15], [22] are two methods of estimating the image background that have been used successfully for this purpose. We will summarize these two methods in Sections II-B. In Section III, we propose a novel enhancement technique by background removal method, which is based on modeling the background structure using the fractal model, and subtracting this modeled image from the original image. The performance of the fractal approach will be compared with those of the morphological and wavelet methods.

1) Morphological Operations: Morphological operations can be employed for many image processing purposes, including edge detection, segmentation, and enhancement of images [13], [14]. The beauty and the simplicity of the mathematical morphology approach come from the fact that a large class of filters can be represented as the combination of two simple operations on images: the erosion and dilation. Let Z denote the set of integers and $f(i,j)$ denote a discrete image signal, where the domain set is given by $\{i,j\} \in N_1 \times N_2, N_1 \times N_2 \subset Z^2$ and the range set by $\{f\} \in N_3, N_3 \subset Z$. A structuring element B is a subset in Z^2 with a simple geometrical shape and size. Denote $B^s = \{-b\colon b \in B\}$ as the symmetric set of B and B_{t_1,t_2} as the translation of B by (t_1,t_2), where $(t_1,t_2) \in Z^2$. The erosion $f \ominus B^s$ and dilation $f \oplus B^s$ can be expressed as [43]

$$(f \ominus B^s)(i,j) = \min_{t_1,t_2 \in B_{i,j}} (f(t_1,t_2)) \tag{2}$$

$$(f \oplus B^s)(i,j) = \max_{t_1,t_2 \in B_{i,j}} (f(t_1,t_2)). \tag{3}$$

Opening $f \circ B$ and closing $f \bullet B$ are defined as [43]

$$(f \circ B)(i,j) = ((f \ominus B^s) \oplus B)(i,j) \tag{4}$$

$$(f \bullet B)(i,j) = ((f \oplus B^s) \ominus B)(i,j). \tag{5}$$

A gray-value image can be viewed as a 2-D surface in a three-dimensional (3-D) space. Given an image, the opening operation removes the objects, which have size smaller than the structuring element, with positive intensity. With an appropriate structuring element (it is usually considered to be the maximal size of microcalcifications), the spots including microcalcifications can be recovered by taking the residual image $r_1(i,j)$ of the opening

$$r_1(i,j) = f(i,j) - (f \circ B)(i,j), \qquad (i,j) \in N_1 \times N_2. \tag{6}$$

It is appropriate to ignore the negative values on the residual image $r_1(i,j)$, because negative value has nothing to do with the objects of interest, so we take

$$r_2(i,j) = \max(0, r_1(i,j)), \qquad (i,j) \in N_1 \times N_2. \tag{7}$$

This approach belongs to the class of image feature enhancement by background removal.

2) Partial Wavelet Reconstruction: It has been demonstrated [44], [45] that if the filters $h(k)$ and $g(k)$, which are associated with certain mother wavelet $\psi(x)$ and mother scaling function $\phi(x)$, are given, one can decompose the digital signal $c_{j,k}$ at scale j via the following recursive equations:

$$\begin{aligned} c_{j+1,n} &= \sum_k c_{j,k} h(k-2n) \\ d_{j+1,n} &= \sum_k c_{j,k} g(k-2n), \qquad j \geq 0. \end{aligned} \tag{8}$$

As a contrary process, $c_{j,k}$ can be reconstructed by

$$\begin{aligned} c_{j,k} = &\sum_n c_{j+1,n} h(k-2n) \\ &+ \sum_n d_{j+1,n} g(k-2n), \qquad 0 \leq j \leq J-1. \end{aligned} \tag{9}$$

It is convenient to view the decomposition as passing a signal $c_{j,k}$ through a pair of filters H and G with the impulse

responses $\tilde{h}(n)$ and $\tilde{g}(n)$ and downsampling the filtered signals by two, where $\tilde{h}(n)$ and $\tilde{g}(n)$ are defined as

$$\tilde{h}(n) = h(-n), \quad \tilde{g}(n) = g(-n). \tag{10}$$

The pair of filters H and G correspond to the halfband lowpass and highpass filters. The reconstruction procedure is implemented by upsampling the subsignals c_{j+1} and d_{j+1} and filtering with $h(n)$ and $g(n)$, respectively, and adding these two filtered signals together. Usually, the signal decomposition scheme is performed recursively to the output of the lowpass filter $\tilde{h}$. It leads to the pyramid wavelet decomposition. Thus, the wavelet transform provides a multiresolution filter-bank decomposition of a signal with a set of orthonormal bases.

The 2-D wavelet transform can be formed by the tensor product of two one-dimensional (1-D) wavelet transforms along the horizontal and vertical directions [45] if the 2-D wavelet filters are separable. The corresponding 2-D filter sequences can be written as

$$\begin{aligned} h_{LL}(k,l) &= h(k)h(l), \quad h_{LH}(k,l) = h(k)g(l), \\ h_{HL}(k,l) &= g(k)h(l), \quad h_{HH}(k,l) = g(k)g(l) \end{aligned} \tag{11}$$

where the first and second subscripts denote the lowpass or highpass filtering in the x and y directions, respectively.

With the 2-D wavelet filters, the image can be decomposed into specific subimages which contain information in different frequency regions. Therefore, one can reconstruct the specific information by partially selecting specific subimages. For example, in order to enhance microcalcifications in a high-frequency region, one can reconstruct a filtered version of the mammogram by ignoring the subimages which represent the low-frequency background [15], [22].

III. Fractal Modeling Enhancement

A. Theoretical Background

Let us first define an affine transformation in a mathematical fashion [38].

Definition 1: An affine transformation $\tau: \mathcal{R}^n \rightarrow \mathcal{R}^n$ can be written as $\tau(\vec{x}) = A\vec{x} + \vec{b}$, where $A \in \mathcal{R}^{n\times n}$ is an $n \times n$ matrix and $\vec{b} \in \mathcal{R}^n$ is an offset vector. Such a transformation will be contractive exactly when its linear part is contractive, and this depends on the metric used to measure distances. If we select a norm $\|\cdot\|$ in $\mathcal{R}^n$ then $\vec{x} \rightarrow A\vec{x}$ is contractive when

$$\|A\| = \sup_{\vec{x}\in\mathcal{R}^n} \|A\vec{x}\|/\|\vec{x}\| < 1. \tag{12}$$

Let $(\boldsymbol{X}, d)$ denote a metric space of digital images, where $\boldsymbol{X}$ is a set, d: $\boldsymbol{X} \times \boldsymbol{X} \rightarrow \mathcal{R}$ is a given metric. Given a complete metric space $(\boldsymbol{X}, d)$, we can define the metric space $(\mathcal{H}(\boldsymbol{X}), h)$, where $\mathcal{H}(\boldsymbol{X})$ is the space of compact subsets of $\boldsymbol{X}$, and the distance h: $\mathcal{H}(\boldsymbol{X}) \times \mathcal{H}(\boldsymbol{X}) \rightarrow \mathcal{R}$ between two sets A and B is the Hausdorff distance, which is characterized in terms of the metric d. Under these conditions, it can be shown that the metric space $\mathcal{H}(\boldsymbol{X})$ is complete according to the Hausdorf metric [38], [39]. Now let $f \in \mathcal{H}(\boldsymbol{X})$ be an original image to be modeled. The task is to construct a contractive image affine transformation τ, defined from $\mathcal{H}(\boldsymbol{X})$ to itself, for which f is an approximated fixed point which is called an attractor. In other words, we wish to find τ: $\mathcal{H}(\boldsymbol{X}) \rightarrow \mathcal{H}(\boldsymbol{X})$, satisfying the requirement

$$\exists s < 1, \quad \forall f_1, f_2 \in \mathcal{H}(\boldsymbol{X}), h(\tau(f_1), \tau(f_2)) \leq s h(f_1, f_2) \tag{13}$$

such that

$$h(f, \tau(f)) < \delta \tag{14}$$

where δ is a tolerance which can be set to different values according to different applications. The scalar s is called the contractivity of τ. It is shown in Theorem 1 that τ can be a set of contractive mappings τ_i, i.e., $\tau = \cup_{i=1}^{N} \tau_i$. According to the deterministic fractal theory, a set of contractive mappings τ_i is the main part of an iterated function system (IFS). The definition of IFS and Theorem 1 are given as follows [38], [39].

Definition 2: An iterated function system (IFS) consists of a complete metric space $(\boldsymbol{X}, d)$ with a finite set of contraction mappings τ_i: $\boldsymbol{X} \rightarrow \boldsymbol{X}$, with respective contractivity factors s_i, for $i = 1, 2, \cdots, N$, and its contractivity factor is $s = \max\{s_i: i = 1, 2, \cdots, N\}$.

Theorem 1: Let $\{\boldsymbol{X}; \tau_n, n = 1, 2, \cdots, N\}$ be an IFS with contractivity factor s. Then the transformation τ: $\mathcal{H}(\boldsymbol{X}) \rightarrow \mathcal{H}(\boldsymbol{X})$ defined by $\tau(B) = \cup_{n=1}^{N} \tau_n(B)$ *for all* $B \in \mathcal{H}(\boldsymbol{X})$, is a contraction mapping on the complete metric space $(\mathcal{H}(\boldsymbol{X}), h)$ with contractivity factor s. Its unique fixed point, or attractor, $A \in \mathcal{H}(\boldsymbol{X})$, obeys $A = \tau(A) = \cup_{n=1}^{N} \tau_n(A)$ and is given by $A = \lim_{n\rightarrow\infty} \tau^{on}(B)$ for any $B \in \mathcal{H}(\boldsymbol{X})$. τ^{on} denotes n iterations of the map τ.

With the definition of IFS and Theorem 1, one can state the important property of IFS in the following theorem.

Theorem 2 (The Collage Theorem): Let $(\boldsymbol{X}, d)$ be a complete metric space. Let $L \in \mathcal{H}(\boldsymbol{X})$ be given, and let $\epsilon \geq 0$ be given. Choose an IFS $\{\boldsymbol{X}; (\tau_0), \tau_1, \tau_2, \cdots, \tau_N\}$ with contractivity factor $0 \leq s < 1$, so that

$$h\left(L, \bigcup_{n=0}^{N} \tau_n(L)\right) \leq \epsilon. \tag{15}$$

Then $h(L, A) \leq \epsilon/(1-s)$, for all $L \in \mathcal{H}(\boldsymbol{X})$, where A is the attractor of the IFS.

The proof of the Collage Theorem can be found in [38]. The Collage Theorem shows that, once an IFS is found, i.e., τ is known such that $h(f, \tau(f)) < \delta$ is satisfied, then from any given image f_0 and any positive integer n, one can get

$$h(f, \tau^{on}(f_0)) \leq \frac{1}{1-s} h(f, \tau(f)) + s^n h(f, f_0). \tag{16}$$

Since $s < 1$, we see that after a number of iterations, the constructed image $f_n = \tau^{on}(f_0)$ will be close visually to the original image f.

The key point of fractal modeling is to explore the self-similarity property of images. Real-world images are seldom self-similar, so it is impossible to find a transformation τ for an entire image. But almost all real images have a local self-similarity. We can divide the image into n small blocks, and

for each block find a corresponding τ_i. So finally, we can define $\tau = \cup_{i=1}^{n} \tau_i$.

Now we introduce a mathematical representation for digital gray-level images. Let $N_1 = [0, 1, \cdots, M], N_2 = [0, 1, \cdots, N], N_3 = [0, 1, \cdots, L]$, respectively, then for any digital gray-level image $f(k,l)$, we have $(k, l, f(k,l)) \in N_1 \times N_2 \times N_3$. Let $D_1, \cdots, D_n$ and $R_1, \cdots, R_n$ be subsets of $N_1 \times N_2$, such that $\cup_{i=1}^{n} R_i = N_1 \times N_2$ and $R_i \cap R_j = \phi, i \neq j$. We call R_i the range squares, and D_i the domain squares. We define a set of mixing functions m_i: $N_1 \times N_2 \rightarrow N_1 \times N_2$, such that $m_i(R_i) = D_i$ using an affine mapping. So, τ_i can be defined as

$$\tau_i(f(k,l)) = s_i f(m_i(k,l)) + o_i \tag{17}$$

where s_i is a scaling factor and o_i is an offset factor; they are blockwise constants on each R_i. Also, let us denote $f|_{R_i}$ as the restriction of the function f to the set R_i. The goal is: for each R_i, a $D_i \subset N_1 \times N_2$ and τ_i: $N_1 \times N_2 \times N_3 \rightarrow N_3$ are sought such that

$$d(f|_{R_i}, \tau_i(f)|_{R_i}) \tag{18}$$

is minimized. In practice, we use $d(\cdot, \cdot)$ as the mean square root metric. Let $f_1, f_2 \in \boldsymbol{X}$ be two digital images, then the mean square root metric d_{rms} is given by

$$\begin{aligned} d_{\text{rms}}(f_1, f_2) &= \|f_1 - f_2\|_2 \\ &= \sqrt{\sum_k \sum_l (f_1(k,l) - f_2(k,l))^2}. \end{aligned} \tag{19}$$

B. Algorithm Implementation

1) Fractal Modeling: Given an $N_1 \times N_2$ pixels N_3 gray-levels digital image, let $\boldsymbol{R}$ be the collection of subsets of $N_1 \times N_2$ from which the R_i are chosen, and let $\boldsymbol{D}$ be the collection of subsets of $N_1 \times N_2$ from which the D_i are chosen. The set $\boldsymbol{R}$ is chosen to consist of 8×8, 16×16, 32×32 pixels of nonoverlapping subsquares of $N_1 \times N_2$. The set $\boldsymbol{D}$ consists of 16×16, 32×32, 64×64 pixels of overlapping subsquares of $N_1 \times N_2$. That is, only domains D_i with a block side twice that of the ranges R_i are allowed, resulting in contraction in the x-y plane. Therefore, each range pixel in R_i corresponds to a 2×2 pixel area in the corresponding domain D_i. The average of the four domain pixel intensities is mapped to the area of the range pixel when computing $\tau_i(f)$. Now, for each R_i, search for all of $\boldsymbol{D}$ to find a $D_i \in \boldsymbol{D}$ which minimizes (18), that is, find the part of the image that looks most similar to that of R_i. Note that each D_i can be rotated to four orientations and flipped and rotated into four other orientations.

Minimization of (18) can be divided into two steps. First, it is necessary to find the optimal s_i and o_i for τ_i. For each $D_i \in \boldsymbol{D}$, we compute the optimal s_i and o_i using the least squares estimation method. From (18), we construct an unconstrained optimization problem as follows:

$$\min \|f(k,l)|_{(k,l) \in R_i} - (s_i \overline{f}(k,l)|_{(k,l) \in D_i} + o_i)\|_2^2 \tag{20}$$

where

$$\begin{aligned} &\overline{f}(k,l) \\ &\quad = \frac{f(k,l) + f(k+1,l) + f(k,l+1) + f(k+1,l+1)}{4} \end{aligned} \tag{21}$$

for all $(k,l) \cup (k+1,l) \cup (k,l+11) \cup (k+1,l+1) \in D_i$. Thus, (20) can be rewritten as

$$\min e_i = \min \sum_k \sum_l (f(k,l) - (s_i \overline{f}(k,l) + o_i))^2. \tag{22}$$

Through solving $\partial e_i / \partial s_i = 0$ and $\partial e_i / \partial o_i = 0$, we get the optimal values of s_i and o_i as shown in (23) at the bottom of the page

$$\hat{o}_i = \frac{\sum_k \sum_l \overline{f}(k,l) - \hat{s}_i \sum_k \sum_l f(k,l)}{N} \tag{24}$$

where N is the total number of pixels in R_i. We put $\hat{s}_i, \hat{o}_i$ into (22), and obtain the minimum error $\hat{e}_i$. Then, we set a uniform tolerance $\delta_i = \overline{\delta}$, and select the best $D_i \in \boldsymbol{D}$, such that $\hat{e}_i < \overline{\delta}$.

Suppose there is a cluster of microcalcifications or some single isolated ones on the image block above R_i, our intention is to find an area D_i on which the image has a similar structure as on R_i, but does not have similar microcalcification patterns. Then when a difference between the original image and modeled image is taken, the microcalcifications will be enhanced. This means that when searching for D_i, the suitable D_i should not cover the region of R_i. In our algorithm, for each given R_i, we constrain the search way of D_i by $R_i \cap D_i = \phi$.

The modeling process is summarized in the following algorithm.

Step 1) Initially, the range squares R_i are chosen to be nonoverlapping subsquares of size 32×32. A search is then performed for the domain squares which best minimized (22) and satisfied the constraint of D_i by $R_i \cap D_i = \phi$.

Step 2) If the value of (22) is less than a predetermined tolerance, then the corresponding D_i and τ_i are stored and the process is repeated for the next range square. If not, the range square is subdivided

$$\hat{s}_i = \frac{N \sum_k \sum_l f(k,l) \overline{f}(k,l) - \left(\sum_k \sum_l f(k,l) \right) \left(\sum_k \sum_l \overline{f}(k,l) \right)}{N \sum_k \sum_l f^2(k,l) - \left(\sum_k \sum_l f(k,l) \right)^2} \tag{23}$$

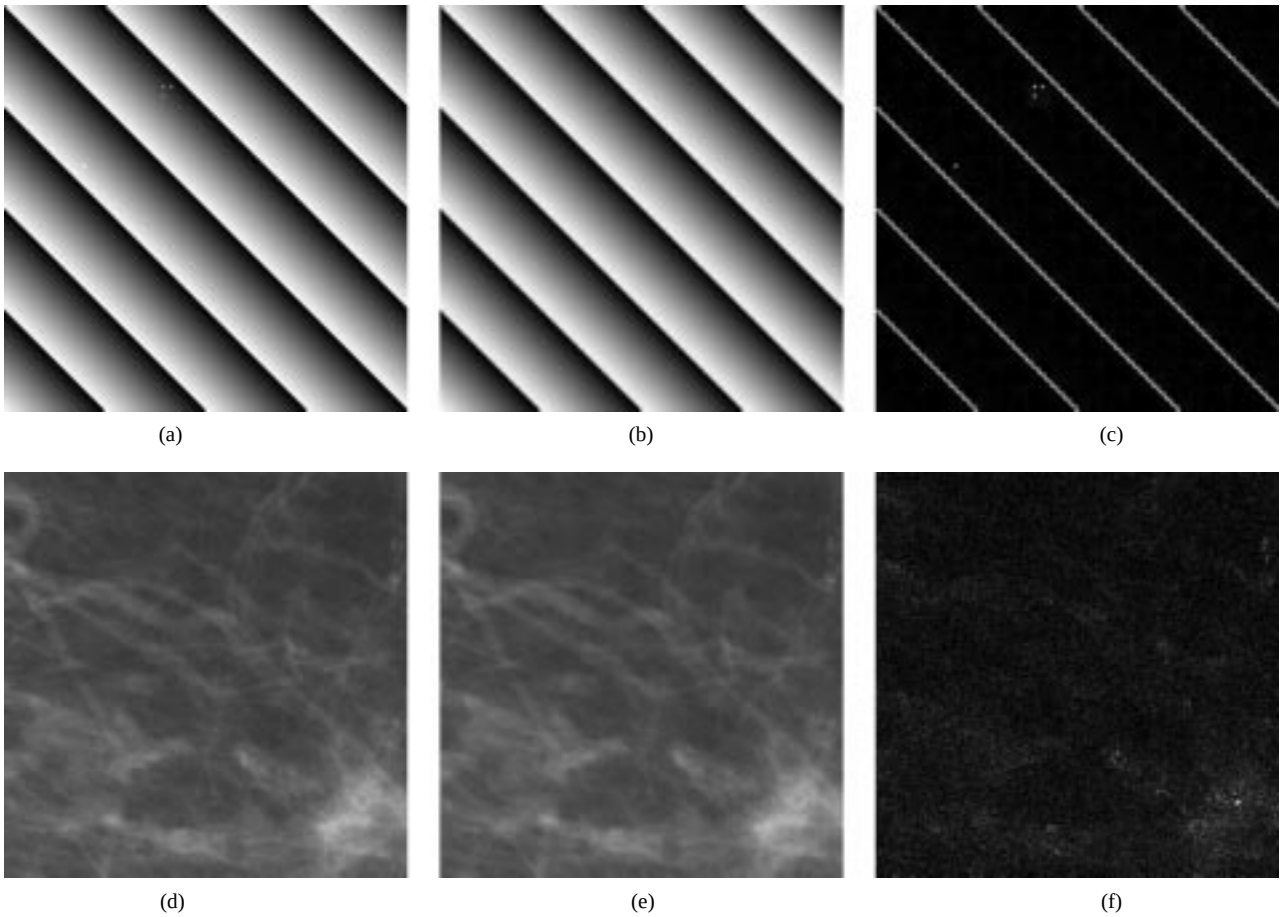

(a) (b) (c)

(d) (e) (f)

Fig. 1. The modeling and enhancement results of the simulated texture image and one real mammogram using the fractal modeling approach. (a) Original image, (b) modeled image, (c) enhanced image, (d) original mammogram, (e) modeled mammogram, and (f) enhanced mammogram.

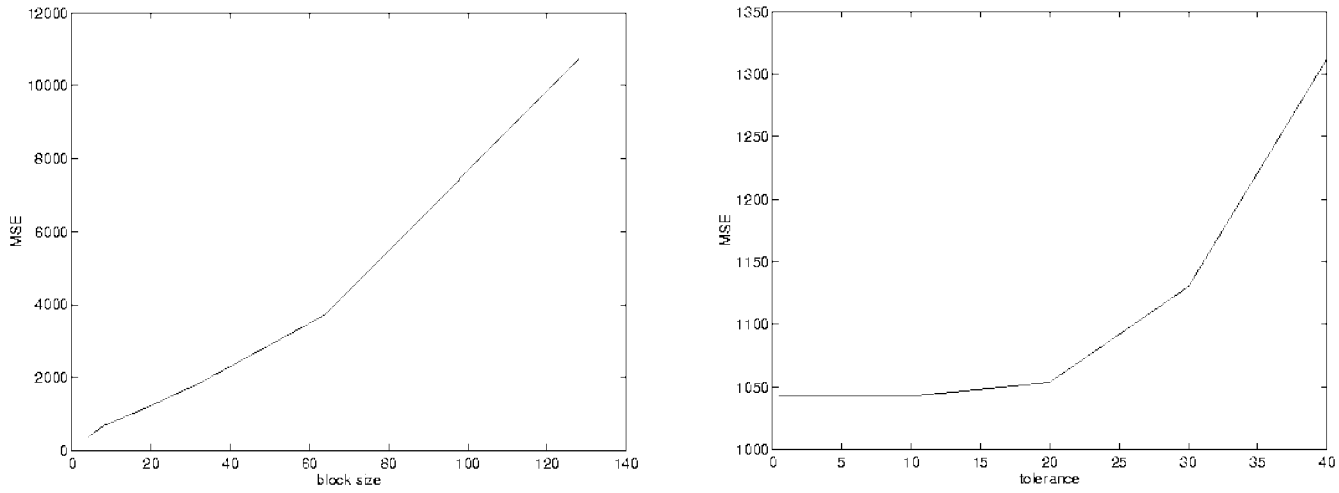

(a) (b)

Fig. 2. The effects on the modeled image with different tolerances and block sizes. (a) The plot of MSE between the original and modeled mammogram with different block size $R_i, \overline{\delta} = 10.0$. (b) The plot of MSE between the original and modeled mammogram with different tolerance $\overline{\delta}, R_i = 8$.

into four equal squares. This quadtreeing process is repeated until the tolerance condition is satisfied, or a range square of minimum size (here we set 8×8 pixels) is reached.

Step 3) The process is continued until the whole image is modeled. A choice of D_i, along with a corresponding s_i and o_i, determines the τ_i on R_i. Once all τ_i are found, we can define $\tau = \cup_{i=1}^{n} \tau_i$, such that $d(f, \tau(f)) < \delta$, where $\delta = n\overline{\delta}$, and n is the block number of R_i.

Step 4) Finally, based on the Collage Theorem, the modeled image can be easily obtained by performing

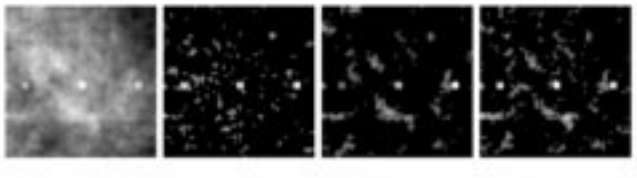

(a) (b) (c) (d)

Fig. 3. The enhancement results of the simulated spots on normal breast tissue background: (a) original ROI, (b) enhancement by the fractal approach, (c) enhancement by the wavelet approach, and (d) enhancement by the morphological approach.

TABLE I
ENHANCEMENT EVALUATION OF PHANTOM IMAGE

Phantom	original	fractal	wavelet	morphology
σ	104.49	29.04	29.77	46.25
C	0.0349	0.7470	0.7410	0.6997
CII		21.39	21.22	20.04
$PSNR$	1.7527	5.9073	6.1106	5.2989
$ASNR$	0.5883	2.6414	1.8697	1.9067

TABLE II
BACKGROUND NOISE EVALUATION

ROIs	σ_{orig}	σ_{frac}	σ_{wave}	σ_{morph}
Mammogram1	38.75	6.95	7.29	6.37
Mammogram2	59.44	14.15	27.98	28.23
Mammogram3	285.04	39.79	66.33	60.82
Mammogram4	101.37	17.87	39.94	22.60
Mammogram5	93.28	17.60	33.39	31.88
Mammogram6	352.95	55.36	95.22	70.27
Mammogram7	154.83	31.16	53.84	62.75
Mammogram8	374.99	44.93	87.53	70.45
Mammogram9	291.30	40.83	66.60	62.08
Mammogram10	180.43	24.04	51.19	41.96
Mammogram11	224.24	18.95	21.62	15.59
Mammogram12	93.78	20.98	89.76	62.61
Mammogram13	274.23	49.63	88.97	48.73
Mammogram14	126.92	12.57	20.78	20.12
Mammogram15	62.27	20.65	29.63	25.49
Mammogram16	70.77	21.39	59.86	40.87
Mammogram17	78.01	21.56	61.73	32.32
Mammogram18	22.68	5.08	9.13	6.71
Mammogram19	96.37	17.34	93.69	60.43
Mammogram20	128.68	11.71	18.62	18.68
Mammogram21	182.27	22.61	42.67	33.99
Mammogram22	168.84	23.99	93.03	49.06
Mammogram23	182.71	30.20	80.26	64.78
Mammogram24	34.97	8.37	13.04	20.44
Mammogram25	39.96	15.85	26.08	28.30
Mammogram26	32.94	4.37	10.99	8.96
Mammogram27	128.39	25.26	89.06	68.45
Mammogram28	128.24	20.52	99.72	67.37
Mammogram29	85.46	23.10	60.41	47.67
Mammogram30	148.46	20.28	72.83	31.06
Mean	141.42	22.90	53.70	40.30

the iteration for any starting image of the same size according to D_i and τ_i. The iteration stops while the predetermined tolerance between the original image and modeled image is achieved.

2) Enhancement of Microcalcifications: Based on the above algorithm development, we can enhance microcalcifications by using the fractal modeling approach. Let $f(k,l)$ be the original image, and $g(k,l)$ be the modeled image after n iterations. The procedure is summarized as follows.

TABLE III
CONTRAST EVALUATION

ROIs	C_{orig}	C_{frac}	C_{wave}	C_{morph}
Mammogram1	0.0975	0.6489	0.6265	0.5061
Mammogram2	0.1264	0.8806	0.8048	0.5581
Mammogram3	0.0766	0.7764	0.6231	0.7731
Mammogram4	0.1141	0.8596	0.8326	0.8819
Mammogram5	0.0678	0.8588	0.7771	0.8458
Mammogram6	0.1413	0.6952	0.4473	0.4102
Mammogram7	0.1879	0.7420	0.7382	0.6677
Mammogram8	0.1542	0.8471	0.8156	0.6679
Mammogram9	0.1455	0.8491	0.7892	0.7849
Mammogram10	0.0090	0.6450	0.3916	0.5402
Mammogram11	0.0410	0.9032	0.8644	0.8199
Mammogram12	0.0947	0.7542	0.2999	0.5570
Mammogram13	0.4022	0.9874	0.8742	0.9943
Mammogram14	0.0470	0.9677	0.9145	0.9164
Mammogram15	0.6426	0.9918	0.9838	0.9838
Mammogram16	0.2787	0.9328	0.9051	0.8763
Mammogram17	0.2797	0.9545	0.8594	0.9327
Mammogram18	0.2222	0.8947	0.8417	0.8690
Mammogram19	0.4425	0.9418	0.7900	0.8792
Mammogram20	0.0591	0.9566	0.8462	0.8041
Mammogram21	0.4140	0.9537	0.9719	0.9497
Mammogram22	0.2050	0.8486	0.7249	0.8187
Mammogram23	0.1065	0.6755	0.5615	0.6482
Mammogram24	0.1866	0.9470	0.9335	0.8935
Mammogram25	0.1493	0.8669	0.8357	0.7340
Mammogram26	0.0167	0.9891	0.8953	0.9348
Mammogram27	0.1796	0.9322	0.8096	0.9000
Mammogram28	0.2367	0.9662	0.8733	0.8491
Mammogram29	0.2647	0.9588	0.8639	0.9149
Mammogram30	0.3646	0.9692	0.8951	0.9687
Mean	0.1918	0.8732	0.7797	0.7960

Step 1) First, we take the difference operation between $f(k,l)$ and $g(k,l)$

$$f_1(k,l) = f(k,l) - g(k,l), \qquad (k,l) \in N_1 \times N_2 \tag{25}$$

where $f_1(k,l)$ is the residue image.

Step 2) It is appropriate to ignore the negative value of the difference image $f_1(k,l)$, because negative part of $f_1(k,l)$ does not contain any information about spots (including microcalcifications) brighter than the background, so we take

$$f_2(k,l) = \max(0, f_1(k,l)), \qquad (k,l) \in N_1 \times N_2 \tag{26}$$

where $f_2(k,l)$ is the enhanced image from which background structures are removed.

Step 3) Image $f_2(k,l)$ contains useful signals and noises. Below a certain threshold T, any signal is considered unreliable. The threshold T is estimated from the image itself as α times the global standard deviation of the noise in an image $f_2(k,l)$. Thus, the value of α is the same for all images, but T depends on each individual image. T can be determined by a two-step estimation process. First the standard deviation of the whole image $f_2(k,l)$ is taken, and the initial threshold T_0 is chosen to be about 2.5

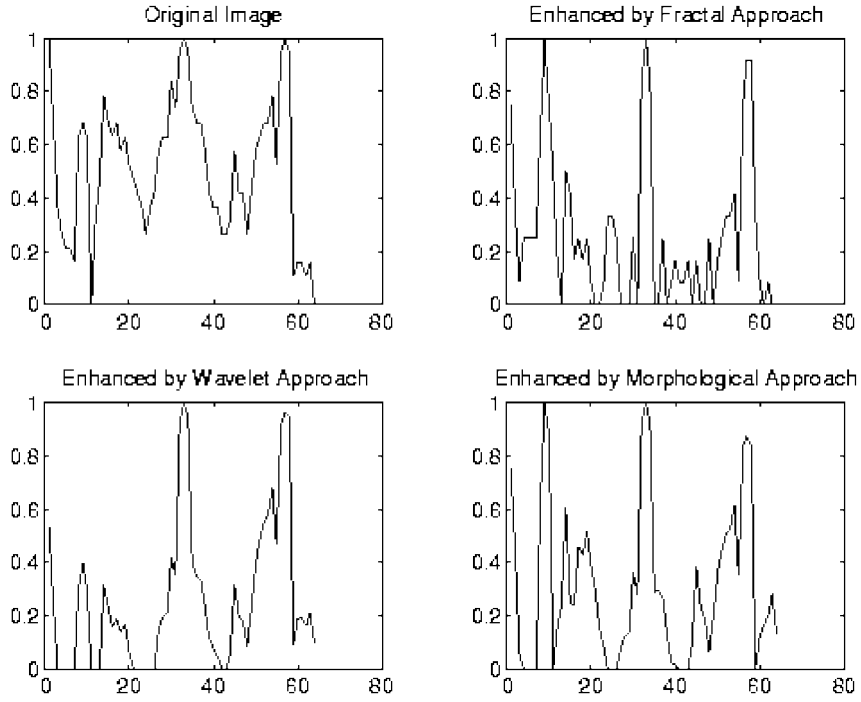

Fig. 4. The 1-D profiles of original spots embedded on normal breast tissue background and enhanced results by the fractal, wavelet, and morphological approaches. The corresponding images is shown in Fig. 3.

times this global standard deviation. Second, only those pixels in which the gray values are below the initial threshold are used to recalculate the standard deviation of the noise. This is a simplified version of a robust estimation of the standard deviation of noise [46]. The final threshold T is determined by adjusting the value of α so that no subtle cases are missed using human judgement. In our study, we found empirically that $\alpha = 3$ is a suitable choice. The final enhanced image $f_3(k,l)$ is

$$f_3(k,l) = \begin{cases} f_2(k,l), & f_2(k,l) \geq T \\ 0, & f_2(k,l) < T. \end{cases} \qquad (27)$$

IV. Evaluation Results and Discussion

Thirty real mammograms with clustered and single microcalcifications were chosen as testing images. The areas of suspicious microcalcifications were identified by a highly experienced radiologist. The selected mammograms were digitized with an image resolution of 100 μm $\times$ 100 μm per pixel by the laser film digitizer (Model: Lumiscan 150). The image sizes are 1792×2560. Each image is 12 b/pixel. In this study, we selected 512×512 regions of interest (ROI's) which contain microcalcifications. In addition, we generated one simple image based on jigsaw function using computer. The simulated image has a simple periodical texture pattern and has a cluster of spots and a single spot embedded in the simulated background structure. This is a suitable example to test the fractal approach.

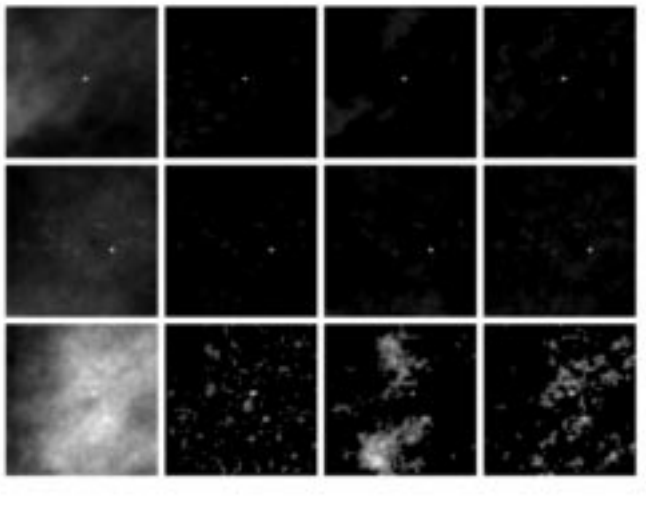

(a) (b) (c) (d)

Fig. 5. The enhancement results of film defects on selected ROI's on mammograms: (a) original ROI, (b) enhancement by the fractal approach, (c) enhancement by the wavelet approach, and (d) enhancement by the morphological approach.

A. Evaluation of Enhancement

In order to evaluate the enhancement results of different approaches, we computed the contrast, the contrast improvement index (CII), the background noise level, the peak signal-to-noise ratio (PSNR), and the average signal to noise ratio (ASNR). The definitions of these indexes are given in the following. All computations were based on the selected local

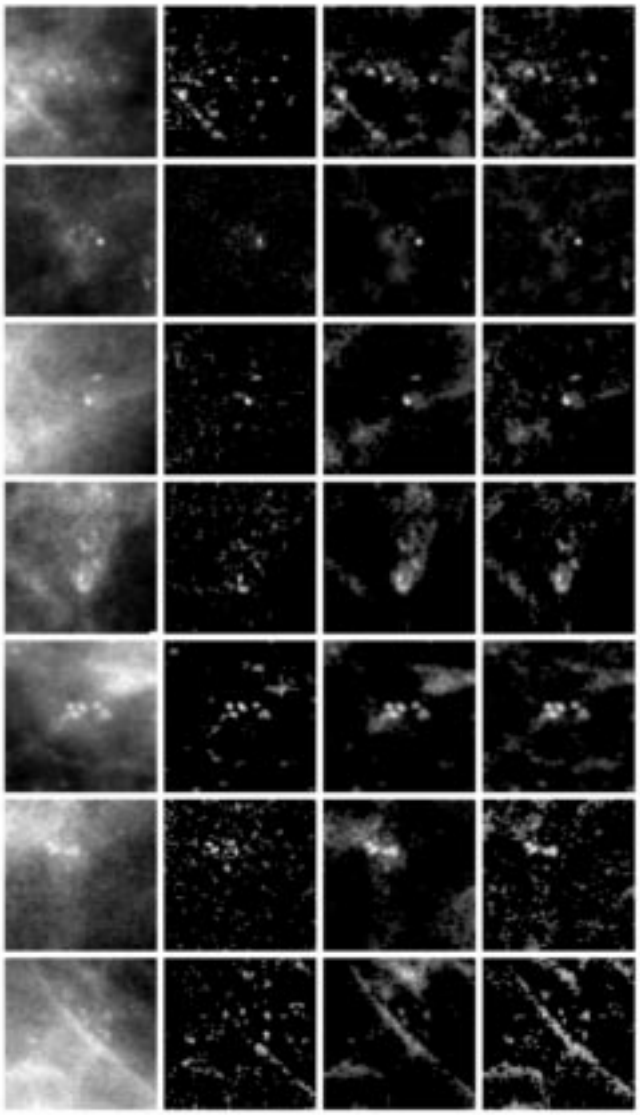

(a) (b) (c) (d)

Fig. 6. The enhancement results of clustered microcalcifications on selected ROI's on mammograms: (a) original ROI, (b) enhancement by the fractal approach (c) enhancement by the wavelet approach, and (d) enhancement by the morphological approach.

ROI's, which contain microcalcifications as well as film artifacts, in the original images, fractal enhanced images, wavelet enhanced images, and morphological enhanced images.

The contrast C of an object is defined by [29]

$$C = \frac{f - b}{f + b} \tag{28}$$

where f is the mean gray-level value of a particular object in the image, called the foreground, and b is the mean gray-level value of a surrounding region, called background. This definition of contrast has been used to evaluate the enhancement in many papers [23], [29]. We computed the contrast of specific ROI's by manually selecting the foreground which contains microcalcifications and background with the help of the radiologist. In order to perform this task, we wrote a program which can let the radiologist trim the local ROI's and choose the foreground with adaptive window size. For the regions which contained clustered microcalcifications, all microcalcifications were selected with different window sizes ($3 \times 3 - 7 \times 7$ pixels), depending on the different size of microcalcifications, and the rest of area was considered as the background. For the regions which contained single microcalcification, the microcalcification was selected as above, and the surrounding region, which had the size three times larger than the size of the foreground, was considered as the background. The positions and sizes of all foreground and background are same for the three different approaches.

TABLE IV
CII EVALUATION

ROIs	CII_{frac}	CII_{wave}	CII_{morph}
Mammogram1	6.65	6.42	5.18
Mammogram2	6.96	6.37	4.41
Mammogram3	10.13	8.31	10.08
Mammogram4	7.53	7.30	7.72
Mammogram5	12.66	11.46	12.47
Mammogram6	4.91	3.16	2.90
Mammogram7	3.94	3.93	3.55
Mammogram8	5.49	5.29	4.32
Mammogram9	5.83	5.43	5.39
Mammogram10	71.52	43.42	59.90
Mammogram11	22.03	21.08	20.00
Mammogram12	7.96	3.17	5.88
Mammogram13	2.45	2.17	2.47
Mammogram14	20.59	19.46	19.50
Mammogram15	1.54	1.53	1.53
Mammogram16	3.35	3.25	3.14
Mammogram17	3.41	3.07	3.33
Mammogram18	4.03	3.79	3.91
Mammogram19	2.13	1.79	1.99
Mammogram12	16.19	14.31	13.60
Mammogram21	2.30	2.34	2.29
Mammogram22	4.14	3.54	3.99
Mammogram23	6.34	5.27	6.09
Mammogram24	5.08	5.00	4.79
Mammogram25	5.81	5.60	4.92
Mammogram26	59.22	53.61	55.98
Mammogram27	5.19	4.51	5.01
Mammogram28	4.08	3.69	3.59
Mammogram29	3.62	3.26	3.47
Mammogram30	2.66	2.46	2.65
Mean	10.59	8.80	9.47

A quantitative measure of contrast improvement can be defined by a CII [23]

$$\text{CII} = \frac{C_{\text{processed}}}{C_{\text{original}}} \tag{29}$$

where $C_{\text{processed}}$ and C_{original} are the contrasts for the ROI's in the processed and original images, respectively.

The background noise level can be measured by the standard derivation σ in the background region which is defined as

$$\sigma = \sqrt{\frac{1}{N}\sum_{i=1}^{N}(b_i - b)^2} \tag{30}$$

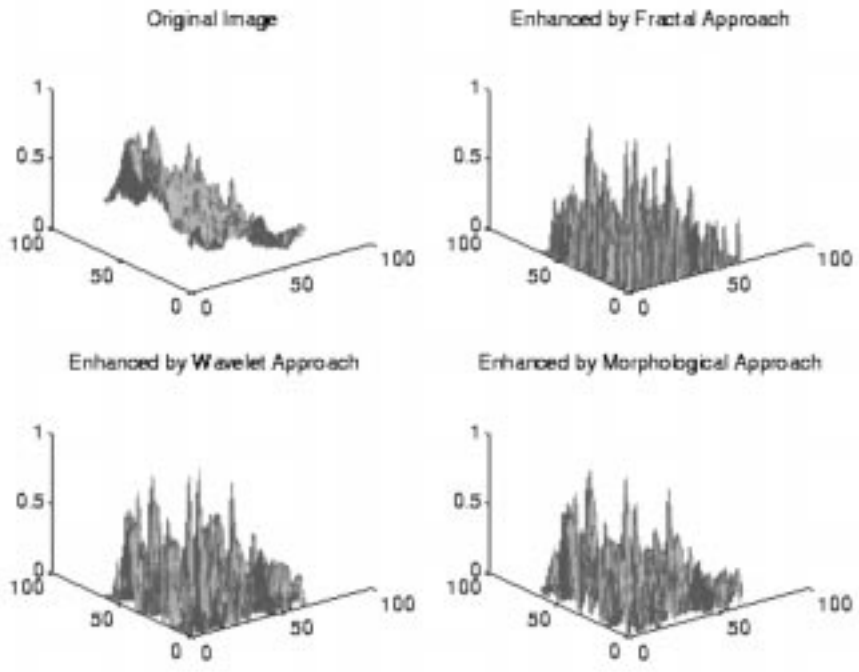

Fig. 7. The 2-D surfaces of original and enhanced clustered microcalcifications on one selected ROI of mammograms correspond to the first row of Fig. 6.

where b_i is the gray-level value of a surrounding background region, and N is the total number of pixels in the surrounding background region.

The evaluation of using the contrast C is not sufficient in our study. The definition of the contrast C does not include the background noise information. Suppose we decrease the gray levels of all pixels by adjusting the window level linearly when we display digital mammograms (radiologists always do this way when they look at digital mammograms), C will increase because $(f-b)$ remains same but $(f+b)$ decreases. In this situation, the noise level of background does not change. If the background is quite smooth, we can still claim that this simple substration operation is a special enhancement. Because, even though $(f-b)$ remains same, the object is more noticeable at low gray-level background according to the property of human visual system [47]. But if the background has large variety (i.e., the noise level is high), the evaluation of using the contrast C is not suitable. Since our work focused on specific microcalcification enhancement and the more interesting work for radiologists is to enhance microcalcifications embedded in inhomogeneous and variable background, we defined two new evaluation indexes, the PSNR and the ASNR. These definitions were based on the general medical physics measurement and accepted by radiologists for the detection of microcalcifications [48], [49].

The PSNR in our work is defined as

$$\text{PSNR} = \frac{p-b}{\sigma} \tag{31}$$

where p is the maximum gray-level value of a foreground.

The ASNR in our work is defined as

$$\text{ASNR} = \frac{f-b}{\sigma}. \tag{32}$$

B. Results and Discussion

We have applied the fractal modeling approach to all real mammograms and the simulated images. Fig. 1 shows the modeled and enhanced results of the simulated image and one of the real mammograms. As we can see in Fig. 1(b) and (e), the background structure in the simulated image and the general mammographic parenchymal and ductal patterns in mammograms were well modeled. In Fig. 1(c) and (f), we can see that all small less-structured objects, which include clusters of microcalcifications, single microcalcifications, and film defects (such as artifacts caused by scratches on the screen or film emulsion), were clearly enhanced. One issue we should mention is that the fractal modeling approach needs enormous computations according to the algorithm implementation. For the 512×512 images we used, the computation time is about 2 min using Dec Alpha Workstation.

In our study, we found that the block size of R_i and predetermined tolerance $\overline{\delta}$ are two very important parameters which can affect the modeling process. We have tried different R_i and $\overline{\delta}$ based on all tested images. Fig. 2 shows the curves of the mean square error (MSE) between the original and modeled mammogram with different R_i and $\overline{\delta}$. As we can see in Fig. 2(a), with fixed $\overline{\delta}$, too large block size would result in visible artificial edge effects on the modeled image, which would increase background noises in the residue image. On the other hand, an R_i of too small size would have less-structured information, therefore, making it difficult to search for the correct D_i. A similar situation occurred when we chose $\overline{\delta}$. In Fig. 2(b), we can see that with fixed R_i, too large $\overline{\delta}$ would introduce more noise and wrong structures on the modeled image. But, too small $\overline{\delta}$ would result in no solution of the search process. In our experiment, we found empirically that

TABLE V
PSNR EVALUATION

ROIs	$PSNR_{orig}$	$PSNR_{frac}$	$PSNR_{wave}$	$PSNR_{morph}$
Mammogram1	1.7846	6.2728	6.3367	5.1478
Mammogram2	7.3597	16.4347	13.7755	13.7713
Mammogram3	1.6667	9.1802	5.8286	7.2354
Mammogram4	10.6939	56.0720	35.7184	47.3344
Mammogram5	6.5640	27.1960	26.0890	27.7183
Mammogram6	2.4290	8.0159	3.8389	6.3515
Mammogram7	3.0944	7.9080	7.3634	4.9245
Mammogram8	2.1348	9.7862	7.2125	8.7916
Mammogram9	2.8060	8.1719	6.3825	6.4690
Mammogram10	0.9189	5.1178	2.3513	3.0158
Mammogram11	1.1478	8.8569	6.3232	7.3137
Mammogram12	1.8459	8.0741	1.8868	3.0398
Mammogram13	7.8330	24.4246	11.1860	21.7692
Mammogram14	2.2541	14.8703	8.7807	8.9332
Mammogram15	17.9734	49.0329	37.6932	43.6230
Mammogram16	5.1008	11.1456	6.5863	8.6843
Mammogram17	6.7567	16.9845	8.3835	15.2593
Mammogram18	2.7102	6.4152	4.0029	7.0701
Mammogram19	9.4995	38.2056	9.7697	14.3518
Mammogram20	1.4912	11.0270	7.8714	8.1237
Mammogram21	7.1226	49.3187	27.4438	41.2678
Mammogram22	3.6102	14.5800	6.0992	10.4983
Mammogram23	2.0740	5.5794	4.2880	4.6258
Mammogram24	4.2373	13.5855	10.4425	7.2959
Mammogram25	3.3153	5.8596	4.7474	3.5598
Mammogram26	3.5498	18.2034	9.1196	11.4857
Mammogram27	3.8389	11.6508	6.0409	7.0979
Mammogram28	4.3347	22.1796	6.3573	7.5792
Mammogram29	5.8837	17.8827	8.3290	8.8423
Mammogram30	3.8841	22.8577	10.9253	19.2964
Mean	4.5971	17.4963	10.3724	11.9312

the suitable block size of R_i is from 32×32 to 8×8, and the range of $\overline{\delta}$ is from 1.0–10.0.

In our experiments, we found that the sharp edge information was also enhanced [it is clearly seen on the simulated texture image in Fig. 1(c)], as well as the bright spots on the image. It implies that this algorithm can also be used for edge detection. On the other hand, it also implies that the IFS fractal compression scheme cannot effectively encode less-structured objects such as microcalcifications, film artifacts, and shape edges. But this method can effectively encode image patterns which have high local self-similarity such as mammographic breast tissue background. The reasons that the IFS cannot effectively model the less-structured objects are as follows: (1) The searching criterion for mapping the domain region D_i to range region R_i is to minimize the least square error to the certain tolerance. For the R_i which contains the less-structured objects, such as sharp edges, the contribution of these less-structured objects to the least square error is small. Therefore, the D_i which contains similar structure as the R_i, but without the less-structured objects, can be found to satisfy the searching criterion. (2) In our proposed modeling algorithm, the searching constraint of D_i by $R_i \cap D_i = \phi$ was added in the encoding procedure. The purpose of the constraint is to find an area D_i on which the image has a similar structure as on R_i, but does not have similar less-structured patterns. On the other hand, it also explains why the less-structured objects cannot be modeled. In our study, we used this property and separated microcalcifications as "compression errors." For the purpose of compression, there are a lot of research [50], [51] on combining fractal method with other compression schemes, this is not an issue in this paper.

For the purpose of evaluating the performance of our proposed fractal enhancement method, we chose for comparison two similar enhancement techniques of background removal: the morphological and partial wavelet reconstruction methods which were described in Section II. In the morphological approach, a disk with a diameter of 11 pixels was chosen as the structuring element B. This is considered to be the maximal size of microcalcifications (1 mm) on our testing mammograms. In the partial wavelet reconstruction method, we investigated the wavelet decomposition of mammograms which contained microcalcifications at different levels by using Daubechies eight-tap orthonormal wavelet filters [44]. We found that all high frequency noise which included film defects was mainly located at the first level of decomposed subimages. On the other hand, all microcalcification information was shown in the second and third levels of decomposed subimages. The low-frequency background structure of the mammogram was concentratedly located in the fourth and higher levels. A similar report was also in [22]. In our study, we decomposed mammograms into four levels, and partially selected subimages in the second and third levels to reconstruct a filtered version of the image. After reconstruction, the microcalcifications

TABLE VI
ASNR EVALUATION

ROIs	$ASNR_{orig}$	$ASNR_{frac}$	$ASNR_{wave}$	$ASNR_{morph}$
Mammogram1	0.7296	1.4267	1.6210	1.5007
Mammogram2	2.2443	5.0962	3.1083	2.8387
Mammogram3	0.6542	2.7932	1.5498	1.9591
Mammogram4	1.0143	4.1203	3.1156	4.0698
Mammogram5	1.4528	2.8024	2.7969	3.2415
Mammogram6	1.4059	2.1200	0.7302	1.4510
Mammogram7	1.6213	2.2672	1.8043	1.7599
Mammogram8	1.1235	2.9150	3.1222	3.6577
Mammogram9	1.9133	3.0026	2.9266	2.1941
Mammogram10	0.2155	0.7295	0.2380	0.5383
Mammogram11	0.7660	1.9497	1.1719	1.9331
Mammogram12	1.0938	2.2888	1.3258	1.4622
Mammogram13	2.7283	7.0324	4.0115	13.9159
Mammogram14	1.1165	3.0143	1.6001	1.6915
Mammogram15	3.5924	8.1347	7.3598	8.2576
Mammogram16	2.2316	3.6978	2.9483	3.6075
Mammogram17	2.5515	4.0988	2.8335	5.6128
Mammogram18	1.4741	2.2837	1.9512	3.1568
Mammogram19	3.3691	7.1242	3.4784	4.6964
Mammogram20	0.9723	4.2210	3.5783	4.1256
Mammogram21	1.1332	11.3812	4.7402	9.0810
Mammogram22	1.7827	4.2108	2.8071	2.9250
Mammogram23	1.0549	1.1376	1.1025	1.7608
Mammogram24	1.2535	3.3498	2.7947	2.6751
Mammogram25	1.7719	2.3735	2.0462	2.0138
Mammogram26	1.7382	4.1465	3.5943	4.6197
Mammogram27	1.5422	3.1912	1.9060	2.7218
Mammogram28	1.4817	5.4504	2.6451	2.0608
Mammogram29	1.4518	5.5112	1.7622	2.5614
Mammogram30	0.9397	4.3092	3.6703	5.2085
Mean	1.5473	3.8727	2.6113	3.5766

were enhanced and low-frequency background structure was removed.

A thresholding algorithm, which was described in Section III, was applied to reduce unreliable noise (the very low contract noise related to the film granularity or due to the subtraction operations) in the fractal, morphological and wavelet approaches. Since some subtle microcalcifications are embedded in very inhomogeneous background, these microcalcifications may be missed after thresholding. So, we used local thresholding based on local gray-level statistics (mean and standard derivation) of image pixels within a specified window to improve the enhancement results in the ROI's.

Except for the real mammograms and the simulated image, we created a phantom mammogram by adding three small spots embedded on the normal breast tissue background. As shown in Fig. 3(a) and its 1-D profile [Fig. 4(a)], the intensities of spots are almost comparable to the intensity of the background, the intensity of the left spot is even lower than its surrounding background. This is a typical subtle case which is easy to be missed by radiologists. After processing all images by the three background removal methods, we cut the local small blocks, which contained microcalcifications and film defects, as the ROI's, from the corresponding original and processed images. The image patches used for one comparison case are in the same location for all original and processed images. The sizes of ROI's are 64×64 pixels. Fig. 3 shows the enhancement results of ROI's in the phantom image. Fig. 4 shows the corresponding 1-D profiles of Fig. 3. Fig. 5 shows the enhancement results of file defects in the mammograms. Fig. 6 shows the enhancement results of clustered and single microcalcifications in the mammograms. The first, second, third, and fourth columns in Figs. 3, 5, and 6 correspond to original ROI's, fractal enhancement, wavelet enhancement, and morphological enhancement, respectively. The results indicated that all three approaches removed the background, and in turn enhanced less-structured spots, including microcalcifications and film defects. We noted that even for the spots embedded in the bright background (such as dense tissues), the enhancement results were still very promising. Furthermore, we observed that the fractal and morphological approaches can remove more background structures than the wavelet approach does, especially for those ROI's with very low contrast compared with the surrounding background (for example, see in the last row of Fig. 6). But the wavelet approach can preserve the overall shape of spots better than the other two approaches. This phenomenon is also clearly observed in Figs. 4 and 7. For example, the normalized intensity of the left spot in Fig. 4 increased more by using the fractal and morphological approaches than those of using the wavelet approach. But, compared with the profile of the original case, the wavelet method reserved the shape of the profile better than those of the other two approaches. It is probably because the wavelet transform has the good time-

frequency localization property, so the wavelet method can keep the dim margins of microcalcifications better than those of the other two approaches.

In order to quantitatively measure the enhancement performance with different approaches, we computed the contrast, the CII, the noise level, the PSNR, and the ASNR. Tables I–VI showed the evaluation results. The values listed in each row in these tables were computed based on the image patches which have the same location for all original and processed images. As we can see from Tables II–VI, different regions have significant differences in evaluation results. These depend on the contrast of microcalcifications to the background, the density, and variety of the background in the original image. In Tables I and II, it is shown that the noise levels of all enhancement ROI's by these three approaches were much lower than the original ROI's. It is reasonable, because background structures were removed. Among these three approaches the noise level of the fractal approach was the lowest. From the other tables, we can see that the averaged results of the contrast, the CII, the PSNR, and the ASNR of the fractal approach were better than those of the wavelet and morphological approaches. All results obtained in this study are very encouraging, and indicate that the fractal modeling and segmentation method is an effective technique to enhance microcalcifications embedded in inhomogeneous breast tissues.

V. Conclusion

In this paper, we proposed a pattern-dependent enhancement algorithm based on the fractal modeling scheme. The proposed approach was applied to enhance microcalcifications in mammograms. We compared the enhancement results with those based on morphological operations and partial wavelet reconstruction methods. Our study showed that in terms of contrast, CII, PSNR, and ASNR, the fractal approach was the best, compared to the other methods. The noise level in the fractal approach was also lower than the other two methods. These results demonstrated that the fractal modeling method is an effective way to extract mammographic patterns and to enhance microcalcifications. Therefore, the proposed method may facilitate the radiologists' diagnosis of breast cancer. We expect that the proposed fractal method can also be used for improving the detection and classification of microcalcifications in a computer system.

References

[1] American Cancer Society, "*Cancer facts and figures—1991*," Tech. Rep., 1991.

[2] R. A. Schmidt and R. M. Nishikawa, "Digital screening mammography," *Principles and Practice Oncol.*, vol. 8, no. 7, pp. 1–16, 1994.

[3] National Cancer Institute of Canada, "*Canadian cancer statistics 1992*," 1992.

[4] R. A. Smith, "Epidemiology of breast cancer," in *Categorical Course in Physics. Technical Aspects of Breast Imaging*, Radiological Soc. North Amer., 1993, pp. 21–33.

[5] E. L. Thurfjell, K. A. Lernevall, and A. A. Taube, "Benefit of independent double reading in a population-based mammography screening program," *Radiol.*, vol. 191, pp. 241–244, 1994.

[6] J. G. Elmore, C. K. Wells, C. H. Lee, D. H. Howard, and A. R. Feinstein, "Variability in radiologists' interpretations of mammograms," *New Eng. J. Med.*, vol. 331, pp. 1493–1499, 1994.

[7] M. Lanyi, *Diagnosis and Differential Diagnosis of Breast Calcifications*. Berlin, Heidelberg: Springer-Verlag, 1988.

[8] E. A. Sickles, "Mammographic features of 300 consecutive nonpalpable breast cancers," *Amer. J. Radiol.*, vol. 146, pp. 661–665, 1986.

[9] H. P. Chan and K. Doi, S. Galhotra, C. J. Vyborny, H. MacMahon, and P. M. Jokich, "Image feature analysis and computer-aided diagnosis in digital radiography. I. Automated detection of microcalcifications in mammography," *Med. Phys.*, vol. 14, pp. 538–548, 1987.

[10] D. H. Davies, D. R. Dance, and C. H. Jones, "Automatic detection of microcalcifications in digital mammograms using local area thresholding techniques," *SPIE Med. Imag.*, vol. 1092, no. 3, pp. 153–159, 1989.

[11] T. Soni, J. R. Zeidler, and W. H. Ku, "Performance evaluation of 2-D adaptive prediction filters for detection of small objects in image data," *IEEE Trans. Image Processing*, vol. 2, no. 3, pp. 327–339, July 1993.

[12] W. Qian, L. P. Clarke, M. Kallergi, H. Li, R. Velthuizen, R. A. Clark, and M. L. Silbiger, "Tree-structured nonlinear filter and wavelet transform for microcalcification segmentation in mammography," *SPIE Biomed. Image Processing and Biomed. Visual.*, vol. 1905, pp. 509–520, 1993.

[13] J. Dengler, S. Behrens, and J. F. Desaga, "Segmentation of microcalcifications in mammograms," *IEEE Trans. Med. Imag.*, vol. 12, no. 4, pp. 634–642, Dec. 1993.

[14] D. Zhao, "Rule-based morphological feature extraction of microcalcifications in mammograms," *SPIE Med. Imag.*, vol. 1095, pp. 702–715, 1993.

[15] S. C. Lo, H. P. Chan, J. S. Lin, H. Li, M. T. Freedman, and S. K. Mun, "Artificial convolution neural network for medical image pattern recognition," *Neural Networks*, vol. 8, no. 7/8, pp. 1201–1214, 1995.

[16] W. Zhang, K. Doi, M. L. Giger, Y. Wu, R. M. Nishikawa, and R. A. Schmidt, " Computerized detection of clustered microcalcifications in digital mammograms using a shift-invariant artificial neural network," *Med. Phys.*, vol. 21, no. 4, pp. 517–524, 1994.

[17] Y. Wu, K. Doi, M. L. Giger, and M. Nishikawa, "Computerized detection of clustered microcalcifications in digital mammograms: Application of artificial neural networks," *Med. Phys.*, vol. 19, pp. 555–560, 1992.

[18] N. Karssemeijer, "A stochastic model for automated detection of calcifications in digital mammograms," in *Proc. 12th Int. Conf. IPMI*, Wye, UK, 1991, pp. 227–238.

[19] N. Karssemeijer, "Recognition of clustered microcalcifications using a random field model," *SPIE Med. Imag.*, vol. 1905, pp. 776–786, 1993.

[20] F. Lefebvre, H. Benali, R. Gilles, E. Kahn, and R. D. Paola, "A fractal approach to the segmentation of microcalcification in digital mammograms," *Med. Phys.*, vol. 22, no. 4, pp. 381–390, 1995.

[21] D. Brzakovic, P. Brzakovic, and M. Neskovic, "An approach to automated screening of mammograms," *SPIE Biomed. Image Processing, Biomed. Visual.*, vol. 1905, pp. 690–701, 1993.

[22] H. Yoshida, K. Doi, and R. M. Nishikawa, "Automated detection of clustered microcalcifications in digital mammograms using wavelet transform techniques," *SPIE Image Processing*, vol. 2167, pp. 868–886, 1994.

[23] A. F. Laine, S. Schuler, J. Fan, and W. Huda, "Mammographic feature enhancement by multiscale analysis," *IEEE Trans. Med. Imag.*, vol. 13, no. 4, pp. 725–740, Dec. 1994.

[24] I. N. Bankman, W. A. Christens-Brry, D. W. Kim, I. N. Weinberg, O. B. Gatewood, and W. R. Brody, "Automated recognition of microcalcification clusters in mammograms," *SPIE Biomed. Image Processing, Biomed. Visual.*, vol. 1905, pp. 731–738, 1993.

[25] N. Karssemeijer, "Adaptive noise equalization and image analysis in mammography," in *Proc. 13th Int. Conf., IPMI'93*, 1993, pp. 472–486.

[26] H. P. Chan, C. J. Vyborny, H. MacMahon, C. E. Metz, K. Doi, and E. A. Sickles, "Digital mammography: ROC studies of the effects of pixel size and unsharp-mask filtering on the detection of subtle microcalcifications," *Investigat. Radiol.*, vol. 22, no. 7, pp. 581–589, 1987.

[27] P. G. Tahoces, J. Correa, M. Souto, C. Gonzalez, L. Gomez, and J. J. Vidal, "Enhancement of chest and breast radiographs by automatic spatial filtering," *IEEE Trans. Med. Imag.*, vol. 10, no. 3, pp. 330–335, 1991.

[28] R. Gordon and R. M. Rangayyan, "Feature enhancement of film mammograms using fixed and adaptive neighborhoods," *Appl. Optics*, vol. 23, no. 4, pp. 560–564, 1984.

[29] W. M. Morrow, R. B. Paranjape, R. M. Rangayyan, and J. E. L. Desautels, "Region-based contrast enhancement of mammograms," *IEEE Trans. Med. Imag.*, vol. 11, no. 3, pp. 392–406, 1992.

[30] A. P. Pentland, "Fractal-based description of natural scenes," *IEEE Trans. Pattern Anal. Machine Intell.*, vol. PAMI-6, no. 6, pp. 661–674, 1984.

[31] M. C. Stein, "Fractal image models and object detection," *SPIE Visual Commun. Image Process. II*, vol. 845, pp. 293–300, 1987.
[32] C. C. Chen, J. S. Daponte, and M. D. Fox, "Fractal feature analysis and classification in medical imaging," *IEEE Trans. Med. Imag.*, vol. 8, no. 2, pp. 133–142, 1989.
[33] C. B. Caldwell, S. J. Stapleton, D. W. Holdsworth, R. A. Jong, W. J. Weiser, G. Cooke, and M. J. Yaffe, "Characterization of mammographic parenchymal pattern by fractal dimension," *SPIE Med. Imag.*, vol. 1092, no. 3, pp. 10–16, 1989.
[34] A. Fourier, D. Fussel, and L. Carpenter, "Computer rendering of stochastic models," *Commun. ACM.*, vol. 25, pp. 371–384, 1982.
[35] J. C. Hart and F. K. Musgrave, "Fractal modeling in 3D computer graphics and imaging," presented at *SIGGRAPH'91*, 1991.
[36] F. J. Malassenet, "Texture coding using a pyramid decomposition," in *Proc. ICASSP'93*, vol. V, pp. 353–356, 1993.
[37] R. Rinaldo and A. Zakhor, "Fractal approximation of images," in *Proc. Data Compression Conf.*, 1993, pp. 451–455.
[38] M. F. Barnsley, *Fractals Everywhere*. New York: Academic, 1988.
[39] M. F. Barnsley, R. L. Devaney, B. B. Mandelbrot, H. O. Peitgen, D. Saupe, and R. F. Voss, *The Science of Fractal Images*. New York: Springer-Verlag, 1988.
[40] A. E. Jacquin, "Image coding based on a fractal theory of iterated contractive image transformations," *IEEE Trans. Images Processing*, vol. 1, no. 1, pp. 18–30, 1992.
[41] E. W. Jacobs, Y. Fisher and R. D. Boss, "Image compression: A study of the iterated transform method," *Signal Processing*, vol. 29, no. 3, pp. 251–263, 1992.
[42] A. K. Jain, *Fundamentals of Digital Image Processing*. Englewood Cliffs, NJ: Prentice-Hall, 1989.
[43] J. Serra, *Image Analysis and Mathematical Morphology*. London, U.K.: Academic, 1982.
[44] I. Daubechies, "Orthonormal bases of compactly supported wavelets," *Communicat. Pure and Appl. Math.*, vol. 41, no. 11, pp. 909–996, 1988.
[45] S. G. Mallat, "A theory for multiresolution signal decomposition: The wavelet representation," *IEEE Trans. Pattern Anal. Machine Intell,*, vol. PAMI-11, no. 7, pp. 674–693, 1989.
[46] P. J. Huber, *Robust Statistic*. New York: Wiley, 1981.
[47] R. C. Gonzalez and P. Wintz, *Digital Image Processing*. Reading, MA: Addison-Wesley, 1987, pp. 16–19.
[48] D. P. Chakraborty, "Physical measures of image quality in mammography," *SPIE Med. Imag.*, vol. 2708, pp. 179–193, 1996.
[49] M. J. Tapiovaara and R. F. Wagner, "SNR and noise measurements for medical imaging: I. A practical approach based On statistical decision theory," *Phys. Med. Biol.*, vol. 38, pp. 71–92, 1993.
[50] R. Rinaldo and G. Calvagno, "Image coding by block prediction of multiresolution subimages," Universita di Padova, Tech.l Rep., 1995.
[51] M. Gharavi-Alkhansari and T. Huang, "Fractal-based techniques for a generalized image coding method," in *Proc. IEEE ICASSP*, 1994.